DOI: 10.1002/ejic.201001297

Au@MOF-5 and Au/MO$_x$@MOF-5 (M = Zn, Ti; x = 1, 2): Preparation and Microstructural Characterisation

Maike Müller,[a] Stuart Turner,[b] Oleg I. Lebedev,[c] Yuemin Wang,[d]
Gustaaf van Tendeloo,[b] and Roland A. Fischer*[a]

Keywords: Metal-organic frameworks / Host-guest systems / Nanoparticles / Catalysts / Gold

The Zn-carboxylate-based porous coordination polymer MOF-5 [$Zn_4O(bdc)_3$] and the metal oxide loaded materials ZnO@MOF-5 and TiO_2@MOF-5 were loaded in a second step with the precursor [ClAuCO] to yield intermediate materials denoted as [ClAuCO]@MOF-5, [ClAuCO]/ZnO@MOF-5 and [ClAuCO]/TiO_2@MOF-5. These composites were decomposed to Au@MOF-5, Au/ZnO@MOF-5 and Au/TiO_2@MOF-5 under hydrogen at 100 °C. The nanoparticle-loaded hybrid materials were characterised by powder X-ray diffraction (PXRD), IR spectroscopy, X-ray photoelectron spectroscopy (XPS) and N_2 sorption measurements, which reveal an intact MOF-5 structure that maintains a high specific surface area. For Au@MOF-5, crystalline Au nanoparticles were distributed over the MOF matrix in a homogeneous fashion with a size of ca. 1–3 nm, evidenced by high resolution transmission electron microscopy. In the case of Au/ZnO@MOF-5, the Au and metal oxide particles of a few nm in size were coexistent in a given volume of the MOF-5 matrix and were not separated in different crystalline MOF particles. For the TiO_2 loaded materials the oxide is preferentially located near the outer surface of the MOF particles, leading to an increase of larger exterior Au particles in comparison to very small interior Au particles as observed for the other materials. Au@MOF-5, Au/ZnO@MOF-5 and Au/TiO_2@MOF-5 were tested in liquid-phase oxidation of alcohols. Preliminary results show a high activity for the Au loaded materials in this reaction. This observation is attributed to the microstructure of the composites with very small Au particles distributed homogeneously over the MOF matrix.

Introduction

Over the past ten years, the literature on metal-organic frameworks (MOFs) has increased rapidly. Owing to their tuneable crystalline structures and unique features such as high pore volumes, high specific surface areas, structural adaptivity and flexibility, much work has been carried out on potential applications, ranging from gas storage[1] and separation[2] to drug release.[3] In addition, MOFs have found increased interest in the field of heterogeneous catalysis.[4] These open framework compounds can act as catalysts themselves, using open metal sites, unsaturated metal centres[5] and catalytically active organic linkers.[6] Additionally, MOFs have attracted attention by introducing extra framework active sites, by functionalizing the MOF host structure[7] and by using MOFs as support materials, i.e. as a host for catalytic active metal species.[8] The MOF is expected to serve as a stabilizing matrix for nanoparticles (NPs) due to caging effects and at the same time provides a tuneable coordination space for influencing reactivity and selectivity.

The loading of MOFs with functional species, e.g. metal complexes, metal salts or metal and metal oxide particles, is usually achieved during synthesis by modification of the MOF mother liquor,[9] or postsynthesis by solution impregnation,[10] solid grinding[11] or gas-phase infiltration[12] of the MOF material. In the case of impregnation of MOFs in solution, metal complexes or salts are diluted in adequate solvents and subsequently used for impregnation. After removing the solvent, the metal precursors are decomposed to the metal by further treatment. We introduced the concept of solvent-free gas-phase infiltration to yield precursor loaded MOF materials, denoted as $[ML_n]_m$@MOF.[12a] In comparison to the impregnation of MOFs in solution and similar to the solid-grinding method,[11] this gas-phase infiltration benefits from the absence of competition between solvent and metal precursor molecules, and therefore allows a much wider range of metal loadings, even above 40 wt.-% metal in a single step. The intermediate, precursor loaded materials $[ML_n]_m$@MOF are subsequently converted to metal@MOF or metal oxide@MOF; e.g. Pd@MOF-5,[13]

---

[a] Organometallics and Materials Chemistry, Ruhr-Universität Bochum,
Universitätsstrasse 150, 44870 Bochum, Germany
Fax: +49-234-32-14174
E-mail: roland.fischer@rub.de
[b] EMAT, Electron Microscopy for Materials Science, University of Antwerp,
2020 Antwerp, Belgium
[c] Laboratoire CRISMAT, UMR 6508, CNRS-ENSICAEN
6 Bd. Marechal Juin, 14050 Caen, France
[d] Department of Industrial Chemistry, Ruhr-Universität Bochum,
Universitätsstrasse 150, 44870 Bochum, Germany

Supporting information for this article is available on the WWW under http://dx.doi.org/10.1002/ejic.201001297.

Ru@MOF-5,[14] Cu@MOF-5,[15] ZnO@MOF-5,[15b] TiO$_2$@MOF-5[16] and even bimetallic@MOF-5,[17] which have been used as catalysts in a variety of reactions. Further treatment of singly loaded MOF materials with suitable precursors in an independent, second loading step offers the possibility of achieving doubly loaded materials as we reported for Cu/ZnO@MOF-5, the first example of this kind of material.[15b] Cu@MOF-5 and Cu/ZnO@MOF-5 were tested as catalysts in methanol synthesis. The initial catalytic productivity of Cu/ZnO@MOF-5 outperformed the productivity of the singly loaded Cu@MOF-5 and peaked at about 60% of an industrial reference catalyst. This result is particularly interesting because of the comparably low Cu loading (1.4 wt.-%) and the small Cu specific surface area <1 m^2 g^{-1} compared to Cu@MOF-5 (13.8 wt.-% Cu; 65 m^2 g^{-1}Cu), suggesting a very efficient interfacial contact between the Cu and ZnO nanoparticles in Cu/ZnO-@MOF-5. Similar to the Cu/ZnO system, Au/TiO$_2$ and Au/ZnO nanocomposite materials are key systems with respect to the strong metal support interaction in heterogeneous catalysis.[17]

Haruta and coworkers have reported a variety of Au@MOF materials and their catalytic properties in the oxidation of alcohols.[18] They demonstrated the deposition of Au particles onto different MOF materials as supports (MOF-5, Cu-BTC, MIL-53, CPL-2) and reported remarkably high catalytic activity in the liquid-phase oxidation of benzyl alcohol and 1-phenyl ethanol. Recently, we reported the synthesis of Au-loaded zeolite imidazolate frameworks (ZIFs) ZIF-8 [Zn(MeIm)$_2$; Im = imidazolate] and ZIF-90 [Zn(ICA)$_2$; ICA = imidazolate-2-carboxyaldehyde] revealing a homogeneous distribution of Au NPs throughout the ZIF matrix and directed anchoring of Au species by the functional groups of ZIF-90.[19] Thus, we became interested in investigating the effect of an additional loading of MOF-5 as the host matrix with ZnO and TiO$_2$ and the size-dispersion and catalytic performance of the Au NPs. This prompted us to study the microstructure of the title materials in some detail in order to find out if the two nanoparticulate components, Au and MO$_x$ (M = Zn, Ti; x = 1, 2), are truly embedded in a single MOF-5 matrix. Microscopic characterisation of the dispersion and location of metal oxides embedded in the MOF matrices has not been investigated up to now, and microscopic evidence of MOF matrices loaded with two different kinds of metal and metal oxide nanoparticles has not been reported. All of our Au-loaded materials, Au@MOF-5, Au/ZnO@MOF-5 and Au/TiO$_2$@MOF-5 were almost inactive in catalytic oxidation reactions. However, upon addition of a base (K$_2$CO$_3$) to the reaction mixture, the composites showed a very high activity towards the oxidation of alcohols.

Results and Discussion

Gas-Phase Loading of MOF-5 and Metal Oxide@MOF-5 with Au Nanoparticles

The first example of gas-phase loading of MOF-5 with Au nanoparticles was reported by Hermes et al. in 2005.[15a] The Au loaded materials showed polydisperse gold particles in a range of 5 to 20 nm, which were probably included in the MOF-5 host, and large amounts of particles on the outer surface of the MOF host, revealed by TEM. In this early report of Au@MOF-5, [MeAuP(CH$_3$)$_3$] was used as a starting material for the preparation of Au NPs. Regarding the composition of the precursor, the use of highly Lewis-basic trimethylphosphane ligands appeared to be problematic. The characterisation of copper loaded MOF-177 using [(η^5-C$_5$H$_5$)CuP(CH$_3$)$_3$] revealed the difficulty of using metal-organic precursors with P(CH$_3$)$_3$ ligands.[12b] After decomposition of the precursor@MOF material, the residual P(CH$_3$)$_3$ coordinates to the Zn$_4$O subunits of the MOF-5 framework as evidenced by ^{13}C magic angle spinning (MAS) NMR spectroscopy. This coordination introduces defect sites in the MOF host. To overcome this problem, chlorocarbonylgold(I), [ClAuCO], has now been identified as an alternative, more suitable volatile precursor for loading MOF-5 with gold.

Loading MOF-5 with [ClAuCO] was achieved using gas-phase infiltration techniques, as reported for the inclusion of other precursors, to yield [ML$_n$]$_m$@MOF.[12a,15a] Due to the high instability of [ClAuCO], it was not possible to carry out full characterisation of [ClAuCO]@MOF-5. As shown in the FTIR spectrum in Figure 1, [ClAuCO] is present in the loaded MOF-5 material, characterised by the weak CO stretching vibration at 2180 cm^{-1}. Further characterisation by PXRD, MAS NMR and elemental analysis failed due to the fast decomposition of [ClAuCO] in the absence of excess carbon monoxide. As a result, an estimation of the amount of absorbed intact precursor molecules was not possible. Owing to this instability, the precursor loaded material [ClAuCO]@MOF-5 was directly converted into Au@MOF-5 by hydrogenation in a hydrogen stream (method A) or under hydrogen pressure (method B).

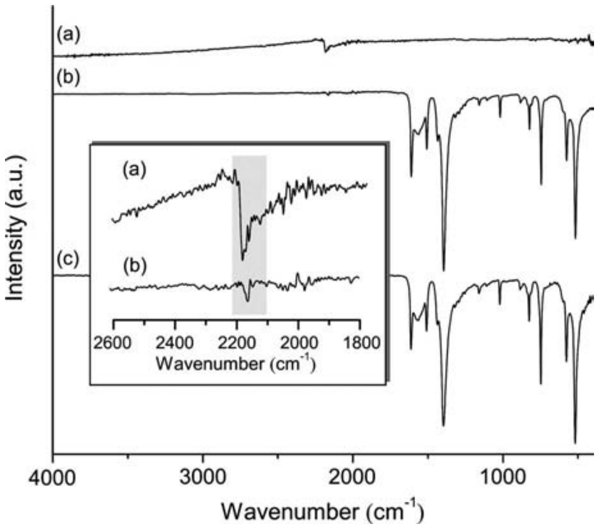

Figure 1. FTIR spectra of [ClAuCO] (a), [ClAuCO]@MOF-5 (b) and pure, activated MOF-5 (c).

In method A, a vial containing [ClAuCO]@MOF-5 was placed in a Schlenk tube and hydrogen (99.999 vol.-%) was passed over the material at elevated temperature (150 °C). The loaded material changed colour from light violet to violet/red. After 6 h, residual ligands and decomposition products were removed under reduced pressure at elevated temperatures. In method B, [ClAuCO]@MOF-5 was transferred to a Fisher–Porter bottle, which was evacuated, filled with 2 bar hydrogen (99.999 vol.-%) and heated to 100 °C for 6 h. A colour change was observed. After decomposition, residual ligands and hydrochloric acid present due to the decomposition reaction were removed in a dynamic vacuum (100 °C). Au@MOF-5 materials with various amounts of Au (1–20 wt.-%) were obtained by varying the amount of [ClAuCO] during the loading procedure. For further characterization, a representative sample with 5.9 wt.-% Au as determined by atomic absorption spectroscopy was used.

Loading MOF-5 with zinc oxide or titania NPs has been reported in detail.[15b,16] Pure and activated MOF-5 is loaded with [$(C_2H_5)_2Zn$] or [Ti(O*i*Pr)$_4$] under reduced pressure and the composite precursor@MOF-5 is converted to ZnO@MOF-5 or TiO_2@MOF-5 in an oxygen stream (4.5 vol.-% O_2 in Ar). The MOF-5 matrix is loaded with a metal oxide in the first step and this intermediate is infiltrated with a metal-organic precursor in the second step. The additional gas-phase loading of the MO_x@MOF-5 materials (ZnO@MOF-5 and TiO_2@MOF-5) was performed with [ClAuCO] to yield a [ClAuCO]/metal oxide@MOF-5 material. Subsequently, these materials were converted into Au/MO_x@MOF-5 by hydrogenation in a Fisher–Porter bottle as described above for Au@MOF-5 (method B). These procedures resulted in doubly loaded Au/ZnO@MOF-5 and Au/TiO_2@MOF-5 composite materials with Au contents of 20 and 15 wt.-%, respectively. All materials retained the crystallinity of MOF-5 as determined by PXRD, IR, TEM, XPS, N_2 sorption isotherms and UV/Vis spectroscopy.

Microstructure Characterisation of Au@MOF-5, Au/ZnO@MOF-5 and Au/TiO_2@MOF-5

Powder X-ray Diffraction

Figure 2 displays the PXRD patterns of Au@MOF-5 prepared by the two different methods described above, metal oxide@MOF-5, Au/metal oxide@MOF-5 and the empty, activated MOF-5 material. The pattern of Au@MOF-5 is dominated by the typical powder pattern of MOF-5, indicating that the crystalline order of the MOF-5 host remains intact after loading. The decomposition of [ClAuCO]@MOF-5 to Au@MOF-5 is likely to yield HCl as a by-product which may degrade the MOF-5 network. However, the Bragg reflections of the loaded MOF-5 do not show any difference to the empty MOF-5 material, indicating that HCl does not significantly degrade the MOF-5 host framework. The main reflections in the range of 2θ = 5–50° do not show any shifts in peak position, but some changes are observed. Inspection of the low angle region reveals small changes in the intensity ratio of the reflections at 2θ = 6.8 and 9.6°. It was shown previously that loading the pores of MOFs with metal complexes, metal nanoparticles and solvents leads to small changes in intensity ratios.[20] The inclusion of atoms with a higher X-ray scattering factor has an influence on the X-ray reflex intensities in comparison to the empty MOF. In addition to the Bragg lines of the MOF-5 host, very broad Bragg lines can be observed in the region of 2θ = 30–90°. These lines, positioned at 2θ = 38.2, 44.4, 64.7 and 77.6°, are assigned to the (111), (200), (220) and (311) lattice spacing of the fcc structure of gold (JPDS No. 00–004–0784). The mean crystalline domain size (coherence length) of the Au particles was estimated to be around 3.3 nm for samples prepared by method A and slightly smaller (3.0 nm) for those prepared by method B (using the Scherrer equation on the 38.2° reflection in both cases). Obviously, the MOF-5 host is locally damaged by particles exceeding the size of the MOF-5 cavity (12 Å). It is known from other porous materials such as zeolites that the size of included particles can exceed the size of the inner pores or channels, causing some local defects in the framework.[21] However, these local defects do not affect the overall crystallinity of the host matrix in such

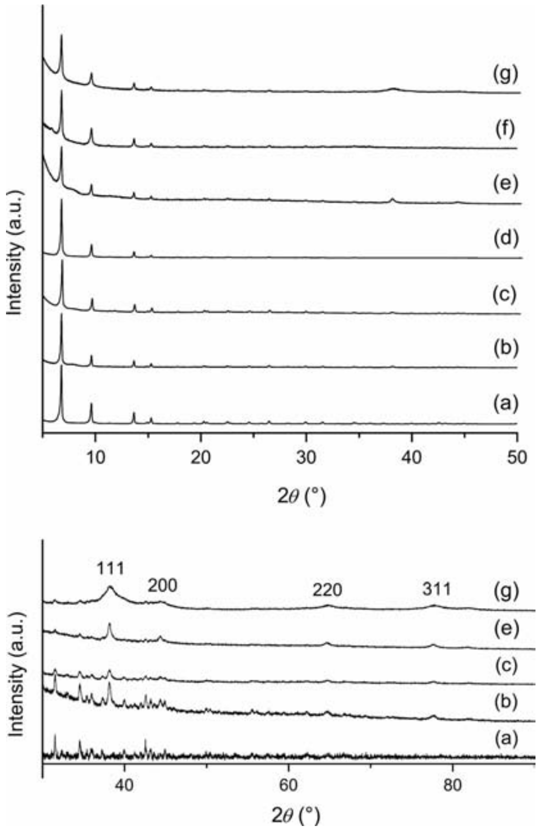

Figure 2. Top: PXRD of pure, activated MOF-5 (a), Au@MOF-5 prepared by method A (b), Au@MOF-5 prepared by method B (c), TiO_2@MOF-5 (d), Au/TiO_2@MOF-5 (e), ZnO@MOF-5 (f) and Au/ZnO@MOF-5 (g). Bottom: enlargement of the region 2θ = 30–90° of MOF-5 (a), Au@MOF-5 prepared by method A (b), Au@MOF-5 prepared by method B (c), Au/TiO_2@MOF-5 (e) and Au/ZnO@MOF-5 indicating the reflexes for crystalline fcc Au^0 (JPDS No. 00-004-0784) (g).

a way that the degradation can be observed in the PXRD pattern of the loaded material in comparison to the empty, activated MOF-5.

Besides the typical pattern of the MOF-5 host, the PXRD patterns of the metal/metal oxide loaded materials exhibit some broad peaks which can be assigned either to the fcc structure of gold (JPDS No. 00–004–0784) or, in the case of Au/ZnO@MOF-5, to the hexagonal wurzite structure of ZnO (Supporting Information).[15b,16] Using the Scherrer equation and assuming spherical particles, the typical crystallite domain size of the Au particles in Au/ZnO@MOF-5 was estimated to be close to 1 nm, which is considerably smaller than that in Au@MOF-5. In contrast, the average crystallite size of the Au particles in Au/TiO$_2$@MOF-5 was calculated to be approximately 3.6 nm.

Transmission Electron Microscopy

Electron microscopy techniques comprising high resolution TEM (HRTEM), electron diffraction (ED), high-angle annular dark-field scanning transmission electron microscopy (HAADF-STEM) and energy-filtered TEM (EFTEM) were applied to provide local structural information for the loaded MOFs. As discussed in previous work, the structure of the MOF-5 framework remains largely intact under low-dose electron illumination (low magnification TEM and ED) but does degrade under the intense electron dose needed for HRTEM imaging.[22] To avoid degradation of the MOF-5 framework as much as possible, the bright field TEM (BFTEM) and HRTEM images of Au@MOF-5 synthesised by method B, presented in Figure 3 were taken using a minimal electron dose. The BFTEM image in Figure 3 (a) shows a typical low-magnification image of Au@MOF-5. The facetted structure of the MOF-5 crystal in the BFTEM image (Figure 3, a) indicates the almost intact structure of the MOF-5 host. Only very few large Au particles (ca. 100 nm in diameter), certainly located outside the matrix, are visible in the image; the rest of the material shows a uniform contrast. In the high resolution images (Figure 3, b–e), a partial degradation of the MOF-5 framework cannot be excluded. Upon closer inspection using HRTEM, the MOF-5 host can be seen to be homogeneously loaded with small particles (approx. 2.7 nm), as shown in Figure 3 (b, c). As any surface enrichment of gold cannot be observed, the Au particles seem to be dispersed throughout the inner pores of the matrix. The FFT (fast Fourier transform) pattern, shown inset in Figure 3 (b), evidences the fcc crystal structure of the gold NPs through the ring at 2.4 Å corresponding to the d$_{111}$ lattice spacing. Two typical individual gold NPs are displayed in Figure 3 (d, e), and the crystalline nature of the gold NPs is immediately clear. The particle in Figure 3 (d) is approximately 2 nm in diameter, with mainly {111}-type surface facets and probably some {200}-type truncation. However, the contrast with the MOF matrix makes a conclusion difficult for particles of this size. The particle in Figure 3 (e) is slightly larger and clearly possesses a truncated octahedral morphology with mainly {111}-type surface facets and some {200}-type truncation. Icosahedral or decahedral particles were not observed by HRTEM imaging. These NPs are all well below 5 nm in diameter as expected from X-ray diffraction, which rules out substantial particle growth during TEM imaging.

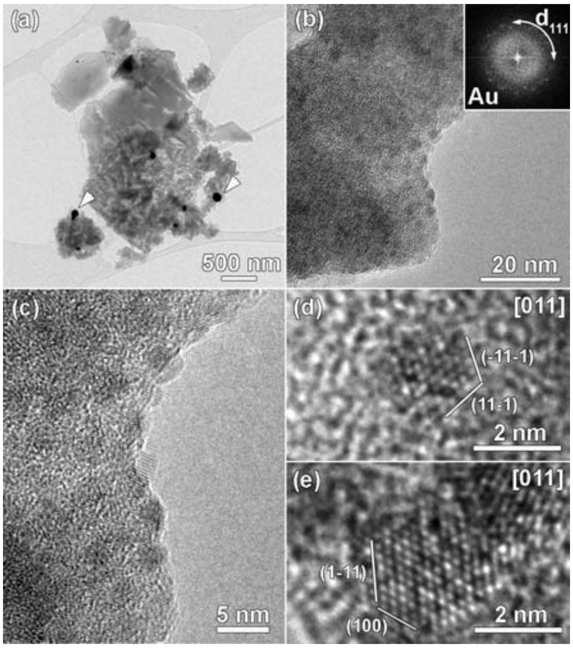

Figure 3. Micrographs of Au@MOF-5; BFTEM image of Au@MOF-5 where only few large Au particles are visible, indicated by arrows (a), HRTEM image showing an even distribution of small Au nanoparticles. The FFT pattern inset evidences the cubic crystal structure of the Au particles through the d$_{111}$ spacing at 2.4 Å (b), enlarged image of the HRTEM image showing that the nanoparticles are all well below 5 nm in diameter (c), 2 nm Au nanoparticle imaged along the [011] zone axis orientation showing typical {111}-type surface planes (d) and 3 nm Au particle imaged along the [011] zone axis orientation with a truncated octahedral morphology with {111} and {100}-type surface planes (e).

Au/ZnO@MOF-5 and Au/TiO$_2$@MOF-5 were also investigated by TEM (Figures 4, 5, 6, and 7). In our earlier reports,[15b,16] it was not possible to prove the existence of nanoparticulate oxide materials in loaded MOF composites due to the TEM techniques applied. By applying HRTEM methods, we can now report the size, location, dispersion and structure of metal oxide@MOF-5 materials for the first time. For Au/ZnO@MOF-5, larger NPs with a size of approximately 5–15 nm can be seen in addition to a large number of small particles well below 5 nm. The ED pattern shown inset in Figure 4 (a) only shows rings corresponding to the Au fcc crystal structure, indicating that the larger particles are probably gold nanoparticles. This assumption was further confirmed by HAADF-STEM (Figure 4, b). Due to the mass-thickness contrast regime present in this type of image, the heavy NPs light up. The larger particles show approximately the same contrast in these images, indicating that they are made of the same material, namely Au.

This result was further confirmed by HRTEM (see below). In all cases, the larger 5–15 nm particles were determined to be gold NPs, presumably on the outer part of the matrix.

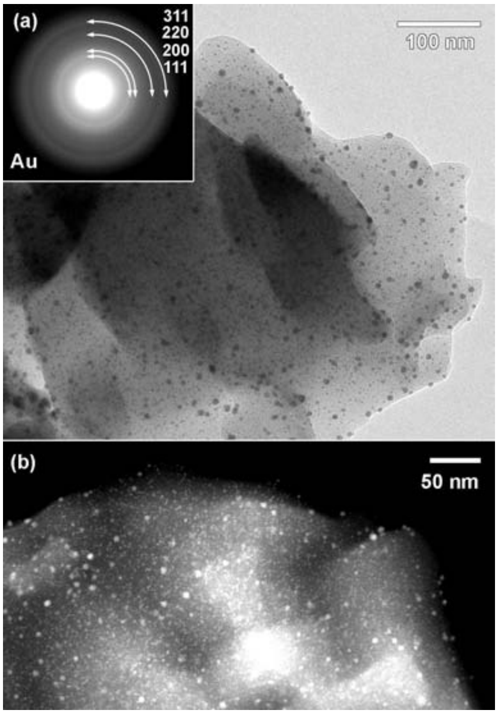

Figure 4. Micrographs of Au/ZnO@MOF-5; BFTEM image of Au/ZnO@MOF-5 crystal showing the presence of large Au nanoparticles and inset rotationally averaged diffraction pattern showing only rings corresponding to the cubic structure of the Au nanoparticles (a) and HAADF-STEM image of the same MOF-5 crystal, all particles above ca. 5 nm are Au nanoparticles showing similar image contrast (b).

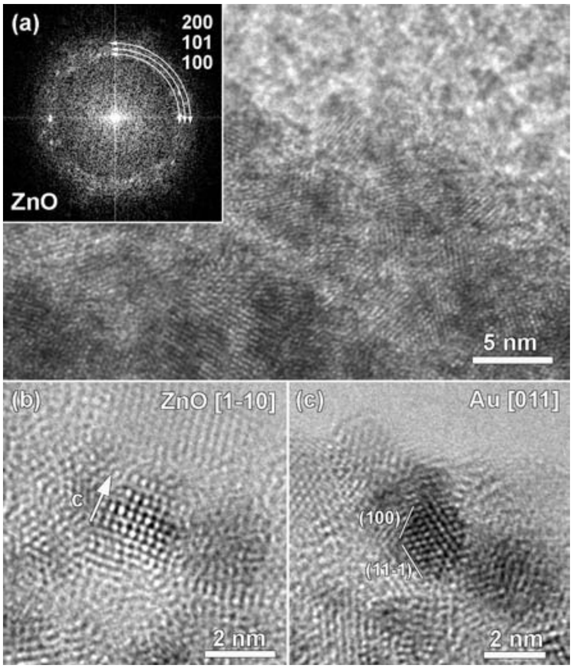

Figure 5. Micrographs of Au/ZnO@MOF-5; HRTEM image of a loaded Au/ZnO@MOF-5 crystal; the crystal is homogeneously loaded with very small, crystalline particles and inset FFT of this HRTEM image evidencing the ZnO wurtzite crystal structure of the small nanoparticles (a), HRTEM image of a ZnO nanoparticle imaged along the [1–10] zone axis orientation (b) and HRTEM image of an Au nanoparticle imaged along the [011] zone axis orientation showing mainly {111} and {100}-type surface planes (c).

HRTEM imaging of the Au/ZnO@MOF-5 crystals indicates that in most cases the MOF-5 framework is homogeneously loaded with very small (<5 nm) crystalline particles. The vast majority of these small particles are ZnO NPs as evidenced through the FFT pattern of a high resolution image of a typical Au/ZnO@MOF-5 crystal shown inset in Figure 5 (a), which only shows rings corresponding to the wurtzite crystal structure of ZnO. However, a small amount of Au particles with particle sizes below 5 nm were observed simultaneously with the ZnO particles. However, most of the Au particles are larger than 5 nm in diameter. A typical 2 nm ZnO NP imaged along the [1–10] zone axis orientation is shown in Figure 5 (b) and a typical 3 nm Au NP imaged along the [011] zone axis orientation is shown in Figure 5 (c).

A typical Au/TiO_2@MOF-5 crystal is imaged in Figure 6 (a). The MOF-5 host can be seen to support large 10–50 nm particles. As was the case for Au/ZnO@MOF-5, the inset ED pattern shows rings corresponding to the Au fcc crystal structure, indicating that particles are indeed gold NPs. HRTEM imaging of the Au/TiO_2@MOF-5 crystals confirms this result. In Figure 6 (b), a typical 25 nm Au nanoparticle is displayed. In Figure 6 (c), poorly crystallised nanoparticles 1–2 nm in diameter can be identified close to the external surface of the MOF crystallite specimen. These nanoparticles are presumed to be TiO_2.

The preferential embedding of the TiO_2 nanoparticles close to or at the MOF-5 surface is confirmed by energy-filtered (EF) TEM imaging of the TiO_2/Au@MOF-5 sample, displayed in Figure 7. In Figure 7 (a), a zero-loss filtered image of a typical crystal is shown. The black spheres are the Au nanoparticles and the titania nanoparticles cannot be easily discerned. However, the position of the TiO_2 particles is immediately clear from the Ti-map obtained using the Ti $L_{2,3}$ edge in Figure 7 (b); the titanium signal follows the contours of the loaded MOF-5 host, indicating a preferential embedding and location of the titania particles at the outer surface of the MOF specimen. This is in contrast to ZnO@MOF-5 materials, where the ZnO nanoparticles are mainly located inside the MOF crystals. This discrepancy could result from the difference in reactivity towards oxygen during the oxidation step. For [$ZnEt_2$], the decomposition in an oxygen stream is rapid and already takes place at room temperature, whereas in the case of [$Ti(O\textit{i}Pr)_4$], the decomposition needs to be performed at elevated temperatures. At conditions >100 °C, diffusion of the intact titania precursor to the outer surface of the MOF crystal is likely and therefore its decomposition is induced preferentially at the outer parts of the MOF host. As a result, the preparation and distribution of small Au particles

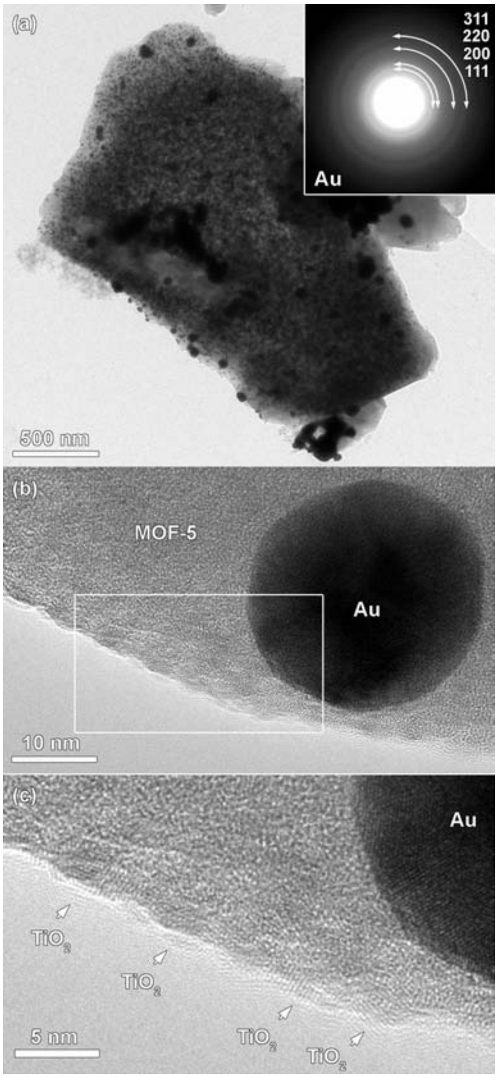

Figure 6. Micrographs of Au/TiO$_2$@MOF-5; BFTEM image showing the presence of large Au nanoparticles and inset is shown a rotationally averaged diffraction pattern showing only rings corresponding to the cubic fcc structure of the Au nanoparticles (a), HRTEM image showing a typical large Au nanoparticle (b) and enlarged image of the region indicated in (b) showing fringe contrast from poorly crystallised TiO$_2$ at the surface of the MOF-5 crystal (indicated by arrows) (c).

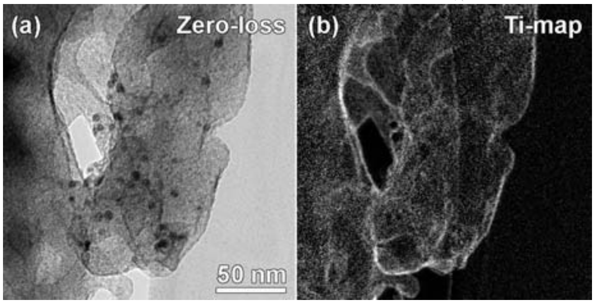

Figure 7. EFTEM of Au/TiO$_2$@MOF-5; zero-loss filtered image of Au/TiO$_2$@MOF-5, the black spheres are Au nanoparticles (a) and Ti-map showing the preferential embedding of titanium at or close to the surface of the MOF-5 host (b).

over the interior of a TiO$_2$ loaded MOF-5 material is more difficult in comparison with a material already loaded with ZnO, and leads to an increase of larger Au particles on the exterior, as represented by a particle size distribution (see Supporting Information).

The estimated particle size for Au particles in Au/oxide@MOF-5 using TEM does not match the size calculated with the Scherrer equation using PXRD data, which is in contrast to that measured and calculated for Au@MOF-5. As the width of the Bragg peaks in the XRD pattern reflect only the coherently scattering domains, the calculated size of Au particles consisting of more than one crystalline domain will correspond to the size of a single domain. For the Au particles in Au/ZnO@MOF-5 and Au/TiO$_2$@MOF-5, the discrepancy in the particle size determined by the two techniques suggests that there are a number of crystalline domains in a single Au particle as shown for detonation nanodiamond.[23] HRTEM analysis confirms this conclusion (see Supporting Information).

Sorption Porperties

The results of N$_2$ sorption characterisation of the materials are displayed in Figure 8 and Table 1. The sorption isotherms show a type I behaviour typical for microporous materials such as MOF-5, with a pore opening diameter of

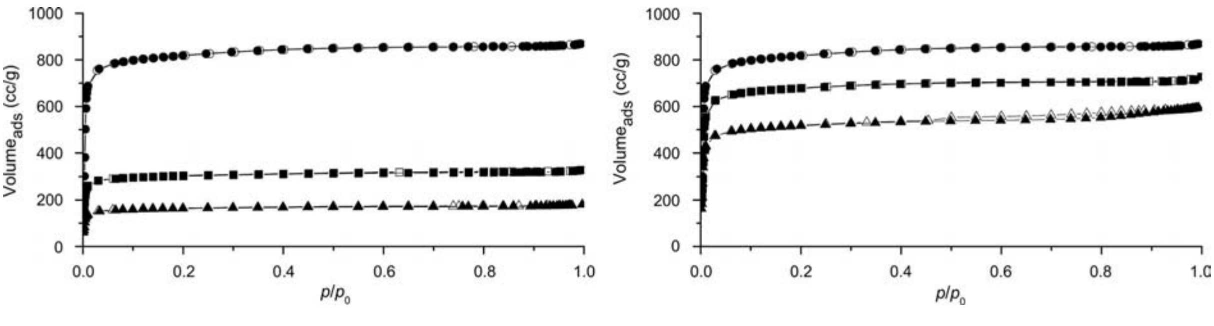

Figure 8. Left: N$_2$ sorption isotherms (77 K) for MOF-5 (filled circle), ZnO@MOF-5 (filled square) and Au/ZnO@MOF-5 (filled triangle). Right: N$_2$ sorption isotherms (77 K) for MOF-5 (filled cicle), TiO$_2$@MOF-5 (filled square), and Au/TiO$_2$@MOF-5 (filled triangle). The adsorption branches are displayed using filled symbols and the desorption branches are displayed using empty symbols.

7.8 Å. By comparing different models, the specific surface area of Au/ZnO@MOF-5 can be estimated to be S_L = 792 m^2/g, S_{BET} = 584 m^2/g. Comparison of empty, unloaded MOF-5 (S_L = 3875 m^2/g, S_{BET} = 3111 m^2/g) with ZnO-loaded MOF-5 systems (S_L = 1340 m^2/g, S_{BET} = 1073 m^2/g), shows that the surface area has clearly dropped. This decrease is a result of the inclusion of additional guest species as already observed for other M@MOF (M = Ru, Au, Pd, Cu) or MO_x@MOF (MO_x = ZnO, TiO_2) materials. Nevertheless, a partial degradation of the MOF-5 host matrix, not seen by XRD, cannot be ruled out. The same behaviour is observed for the titania loaded materials, where the specific surface area of Au/TiO_2@MOF-5 was calculated to be S_L = 2299 m^2/g, S_{BET} = 1842 m^2/g. In comparison, the specific surface area of TiO_2@MOF-5 is calculated to be S_L = 3010 m^2/g, S_{BET} = 2412 m^2/g.

Table 1. Elemental analysis data and results of the N_2 sorption measurements of representative samples of MOF-5, Au@MOF-5, ZnO@MOF-5, TiO_2@MOF-5, Au/ZnO@MOF-5 and Au/TiO_2@MOF-5 prepared by hydrogenation or hydrolysis/annealing of the intermediate precursor@MOF-5 under different conditions (see Experimental Section).

Sample	Elemental analysis, measured [wt.-%]			Specific surface area [m^2/g]	
	Au	Zn	Ti	S_L	S_{BET}
MOF-5	–	33.8	–	3635	2911
Au@MOF-5 (method B)	5.9	27.6	–	3551	2853
ZnO@MOF-5	–	46.6	–	1340	1073
TiO_2@MOF-5	–	30.4	4.2	3010	2412
Au/ZnO@MOF-5	20.7	29.8	–	792	584
Au/TiO_2@MOF-5	15.2	23.1	4.1	2299	1842

Spectroscopic Characterisation of Au@MOF-5, Au/ZnO@MOF-5 and Au/TiO_2@MOF-5

X-ray Photoelectron Spectroscopy (XPS)

To elucidate the nature of the Au and Au/MO_x supported particles, XPS studies were undertaken of both the singly and doubly loaded materials. As shown in Figure 9 zinc-, oxygen- and carbon-related peaks are detected in the XP survey spectra obtained for all the samples. The Zn 2p spectra (Figure 10) exhibit two intense peaks at 1022.5 and 1045.5 eV, which are assigned to the $2p_{3/2}$ and $2p_{1/2}$ components, respectively. Although the Zn 2p core levels are not sensitive to the Zn oxidation state, it can be determined based on the Zn $L_3M_{45}M_{45}$ Auger spectra. The corresponding XPS data (Supporting Information) display a dominant peak at about 987 eV (kinetic energy), revealing the presence of Zn^{2+} cations in the MOF-5 frameworks. The MOF-5 structure is further characterised by the intense hydrocarbon C 1s peak at 285.0 eV and the carboxylate (–COO) C 1s peak at 289.2 eV. The latter species is also identified by the O 1s peak at 532.2 eV, which is the dominant feature observed in the O 1s spectrum for the pure, activated MOF-5 (Figures 10 and 11). Due to the low concentration of the central oxygen (Zn_4O) in comparison to the carboxylate oxygen (COO) (ratio 1:12), it is not possible to observe an additional signal for Zn_4O oxygen atoms. After loading MOF-5 with ZnO, the intensity of the Zn 2p doublet is significantly increased, accompanied by a slight shift of the binding energies to 1021.8 and 1044.9 eV (Figure 10). The deconvolution of the O 1s spectrum results in two peaks at 531.8 and 530.2 eV (Figure 10), which are attributed to the carboxylate and oxide-related species, respectively. These changes in the XPS data reveal the existence of ZnO species in MOF-5. In addition, after ZnO-loading the peak position and line shape of the Zn $L_3M_{45}M_{45}$ Auger spectrum remain nearly unchanged, indicating that no metallic Zn species are formed in the loaded MOF-5. It should be noted that the carboxylate O1s peak shifts by 0.4 eV to lower binding energy with respect to the pure MOF-5. This shift could be attributed to the interaction of loaded ZnO with the MOF-5 framework. For the Au/ZnO@MOF-5 sample, an Au 4f doublet is seen at 84.0 and 87.7 eV in the deconvoluted Au 4f spectrum, which is characteristic for the metallic Au species.

In the case of TiO_2@MOF-5, the presence of TiO_2 in MOF-5 is identified by the deconvoluted O 1s spectrum (Figure 11), which displays the carboxylate O 1s peak at

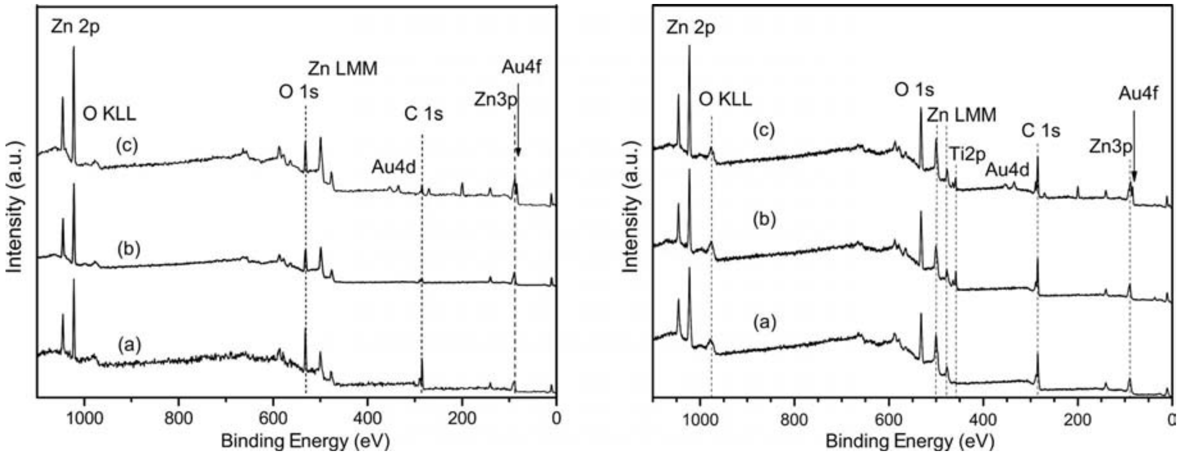

Figure 9. XP survey spectra of the differently modified MOF-5 samples. Left: MOF-5 (a), ZnO@MOF-5 (b) and Au/ZnO@MOF-5 (c). Right: MOF-5 (a), TiO_2@MOF-5 (b) and Au/TiO_2@MOF-5 (c).

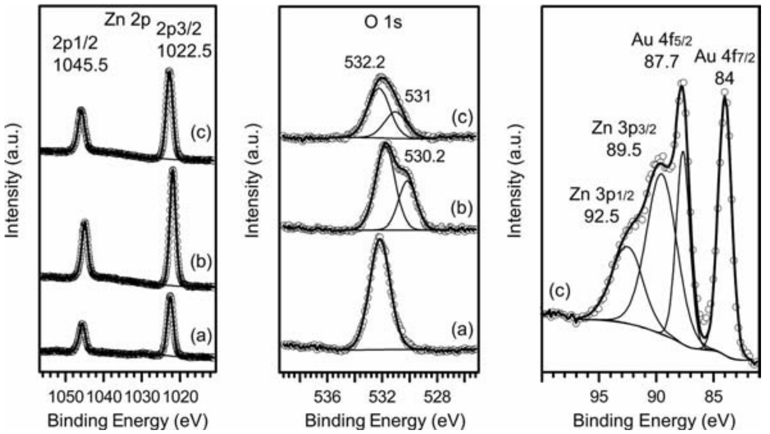

Figure 10. Deconvoluted XP spectra of MOF-5 (a), ZnO@MOF-5 (b) and Au/ZnO@MOF-5 (c).

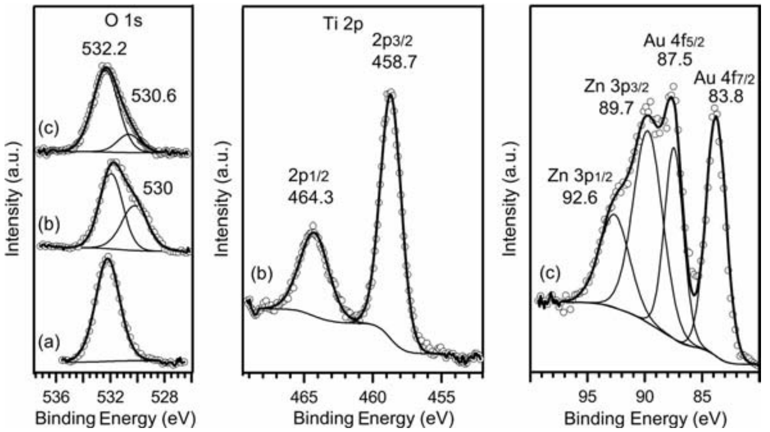

Figure 11. Deconvoluted XP spectra of MOF-5 (a), TiO_2@MOF-5 (b) and Au/TiO_2@MOF-5 (c).

531.8 eV and a new oxide-related O 1s peak at 530.2 eV. The TiO_2 species is further confirmed by the Ti 2p doublet at 458.7 ($2p_{3/2}$) and 464.3 eV ($2p_{1/2}$) characteristic for Ti^{4+} cations. Furthermore, the loading-induced shift of the carboxylate O 1s core level (from 532.2 to 531.8 eV) is also detected for TiO_2@MOF-5 and can be attributed to the interaction of the loaded TiO_2 with the MOF-5 framework. The Au NPs loaded in TiO_2@MOF-5 are identified by a characteristic doublet at 83.8 and 87.5 eV in the deconvoluted Au 4f spectrum. Interestingly, after loading with Au NPs the TiO_2 O 1s peak shifts from 530.0 to 530.6 eV. At the same time, the carboxylate O1s peak shifts to the same binding energy seen for the unloaded MOF-5 (532.2 eV). Similar energy shifts of the O 1s core levels are also observed for the ZnO@MOF-5 and Au/ZnO@MOF-5 samples (Figure 10). These findings might be related to the relatively strong interaction between TiO_2 (or ZnO) and Au NPs loaded in MOF-5.

UV/Vis Spectroscopy

UV/Vis spectra were measured for all samples and the spectra of the loaded materials are displayed in Figure 12. For the Zn-carboxylate-based MOF-5, the empty, activated material is transparent in the region typical for the absorption of zinc oxide or titania and the surface plasmon resonance (SPR) absorption bands of noble metals. MOF-5

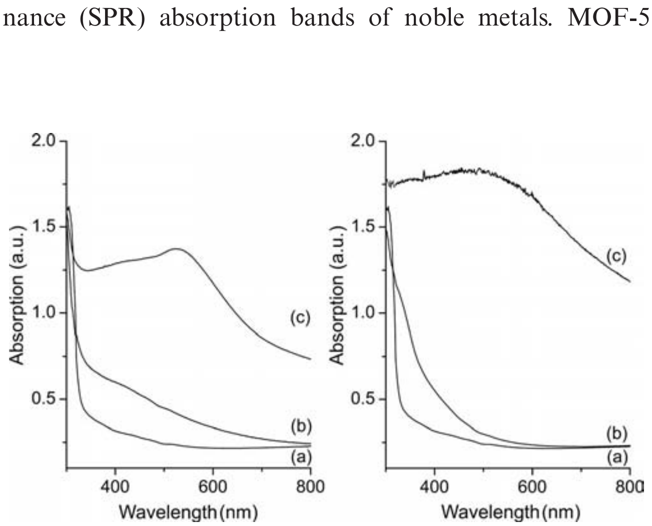

Figure 12. Left: UV-absorption spectra of pure activated MOF-5 (a), TiO_2@MOF-5 (b) and Au/TiO_2@MOF-5 (c); Right: UV-absorption spectra of pure activated MOF-5 (a), ZnO@MOF-5 (b) and Au/ZnO@MOF-5 (c).

shows a strong absorption in the region below 320 nm due to the π→π* excitation of the terephthalic acid linker of the host framework. Upon loading with metal oxide materials, an absorption in the range 400–600 nm is present. In comparison to bulk titania or zinc oxide, the loaded MOF-5 materials show a blueshift of the onset of the metal oxide related absorption. This is due to the embedding of nanometre-sized semiconductor materials, which have properties due to their quantum size structure.[15b,16] It is known that small, crystalline Au particles exhibit a size dependant SPR, which can be observed by UV/Vis spectroscopy.[24]

Upon loading the metal oxide@MOF-5 samples with gold nanoparticles, different absorptions are observed for both Au/ZnO@MOF-5 and Au/TiO_2@MOF-5. In the case of Au/TiO_2@MOF-5, the typical gold SPR is clearly observed around 520 nm, whereas in the case of Au/ZnO@MOF-5 the sharp SPR, typical for gold spheres smaller than 10 nm, is absent.[25] It is known, that the SPR band decreases significantly with decreasing size of Au particles. In the case of Au/ZnO@MOF-5, the absence of the sharp SPR band could be due to the very small size of Au particles below 5 nm. In addition, an interfacial contact between Au and ZnO particles could be the reason for the broadening of the SPR band. As demonstrated by Wang et al., the absorption of Au/ZnO nanocolloids is not just a superposition of the characteristic absorptions of Au and ZnO colloids.[26] As a result of the strong interfacial coupling between the metal and semiconductor particles, the Au-ZnO colloids exhibit a SPR band, which is strongly broadened and redshifted in comparison to pure Au colloids.

Control of Au Nanoparticle Growth and Interfacial Au/MO_x Contact

Together our analytical investigations reveal that the size of the Au nanoparticles in Au/ZnO@MOF-5 and Au/TiO_2@MOF-5 is a function of the preperformed loading with a metal oxide. Although in the case of Au@ZIF-8 and Au@ZIF-90 the organic linkers of the MOF hosts direct the growth of Au particles, our recent work demonstrates the potential of a precedent loading with a metal oxide to influence the size, distribution and the location of metal particles. Depending on the preloaded metal oxide, very small metal/metal oxide particles were distributed homogeneously over the whole material (Au/ZnO@MOF-5) or in a less homogeneous way with the metal oxide located mainly on the outer surface and larger metal particles distributed over the MOF-5 matrix (Au/TiO_2@MOF-5). HRTEM characterisation indicates the positon of both metal and metal oxide particles coexisting in a single MOF-5 particle. Furthermore, XPS and UV/Vis analysis give evidence for interfacial contact between metal and metal oxide nanoparticles in the doubly loaded materials. This contact seems to be more distinct in the case of Au/ZnO@MOF-5 than for the Au/TiO_2 material. Nevertheless, further work has to be carried out to investigate the optical emission properties of Au/MO_x@MOF-5, which could give further hints towards the interfacial contact between Au and metal oxide particles,[26] similar to our work on surfactant-stabilised small Cu/ZnO nanoparticles in colloidal solution.[27] However, this will require homogeneously Au/MO_x loaded MOF-5 single crystals similar to recent work on dye@MOF materials, which are not available at present.[28]

Catalytic Screening of Au@MOF-5, Au/ZnO@MOF-5, and Au/TiO_2@MOF-5 for Liquid Phase Aerobic Alcohol Oxidation

To screen the catalytic activity of the metal/metal oxide@MOF-5 materials, a representative selection of samples was tested in the liquid-phase oxidation of benzyl alcohol. The starting materials and products fit the size of the pore-opening windows of the MOF-5 system and, therefore, should be able to diffuse into the network to access the incorporated metal and metal oxide particles. K_2CO_3 may also access the pores of the MOF host. Interestingly, none of the materials tested showed catalytic activity in the oxidation of benzyl alcohol in absence of a base. However, upon addition of K_2CO_3, the catalytic activity increased dramatically under standard conditions comparable to that reported by Haruta and coworkers.[18] It is known that upon addition of a base, alcohol oxidation reactions are accelerated by deprotonation of the alcohol.[29]

The Au@MOF material derived from the solid grinding method as described in the work of Haruta and coworkers showed a decent activity with a conversion of 68 % after 1 h. A somewhat higher activity was found for our Au@-MOF-5 synthesised by gas-phase infiltration. After 30 min, benzyl alcohol (50 % conversion) was selectively oxidised to methyl benzoate, detected by GC–MS. Compared to Au@-MOF-5, the Au/oxide@MOF-5 catalysts show higher activity and selectivity (see Supporting Information). Surprisingly and in contrast to our data, Haruta and coworkers described the catalytic activity of Au@MOF-5 for the oxidation of benzyl alcohol *without* addition of a base.[18] However, in our work all the catalysts were inactive in the absence of base, even at elevated temperatures. Taking into account the results received by different spectroscopic techniques and microscopic characterisation of our materials, the preliminary data of the catalytic tests are not unexpected. HRTEM analysis evidences the presence of small and evenly distributed Au particles, especially in Au@MOF-5 and Au/ZnO@MOF-5. XPS indicates an interfacial contact between Au/ZnO and Au/TiO_2. Further investigations on the catalytic properties of the Au/MO_x@MOF materials are clearly warranted and a more detailed report on this will be given in the future.

Conclusions

MOF-5 was homogeneously loaded with very small nanocrystalline Au particles throughout the bulk of the support matrix and some larger particles on the exterior by gas-phase infiltration using the precursor [ClAuCO] and subsequent thermal decomposition of [ClAuCO] under a hydrogen atmosphere. In a similar manner the materials ZnO@MOF-5 and TiO_2@MOF-5 were loaded with Au and the Au/MO$_x$@MOF-5 materials obtained also showed a high porosity and intact structure of the MOF-5 host after loading. The microstructural characterisation of Au@-MOF-5 and Au/MO$_x$@MOF-5 revealed that [ClAuCO] is a more suitable precursor than [MeAuP(CH_3)$_3$] for Au loading of MOF-5 and leads to smaller Au particles with a narrower size distribution. Doubly loaded Au/ZnO@MOF-5 shows a positive effect of the presence of ZnO for keeping the Au particles small ($<$ 5 nm) in addition to the caging effect of the MOF-5 matrix. The XPS data indicate Au/ZnO interfacial contact. However, the related material Au/TiO_2@MOF-5 exhibits a less homogeneous distribution of Au and TiO_2 over the host matrix with a preferential location of TiO_2 at the outer surface of the MOF-5. Consequently, there is a broader size distribution of the Au particles, and they are also more prone to be located at the outer surface. Nevertheless, for the first time it is shown that metal and metal oxide particles are not separated in different regions of the crystalline MOF matrix but are both present in one individual crystal. In addition, the catalytic properties of the materials in the liquid-phase aerobic oxidation of alcohols are promising and show the potential to surpass previous results for Au@MOF materials without promoting oxide species. Similar materials with improved microstructures, which can be achieved by reduced loading levels, might be candidates for further studies on solvent-free gas/solid oxidation catalysis. As isoreticular MOFs show catalytic activity in the gas-phase photo-oxidation of propylene,[30] loading with ZnO or TiO_2 nanoparticles and Au/MO$_x$ could significantly influence the activity and selectivity in photo-oxidation reactions.

Experimental Section

Materials and General Techniques: All manipulations were carried out under inert conditions using Schlenk line and glove box techniques (Ar, H_2O, below 1 ppm). [ClAuCO], [(C_2H_5)$_2$Zn] and [Ti(O*i*Pr)$_4$] were purchased from commercial sources and used as received. MOF-5, [Zn_4O(bdc)$_3$], was synthesised following the procedure published by Yaghi et al. with some modifications as described elsewhere.[31] The inclusion compounds [ML$_m$]$_n$@MOF-5 were derived and characterised as described previously.[12b,15b,16]

Analytic and Spectroscopic Methods: FTIR spectra were measured with a Bruker Alpha-P FTIR spectrometer under inert atmosphere in a glove box using a single reflection diamond ATR module. UV/Vis spectra were measured with a Perkin–Elmer Lambda 9 UV/Vis/NIR spectrometer in reflection mode. The samples were introduced into a solid state sample holder for reflection mode under an inert atmosphere in a glove box, and the sample holder was capped with UV-transparent adhesive tape to protect the sample from moisture. Measurements were performed in the diffuse-reflectance mode using $BaSO_4$ as the reference. For the determination of the metal content (Zn, Au, Ti) an AAS apparatus by Vario of type 6 (1998) was employed, and C,H analyses were carried out with a Vario CHNSO EL (1998) instrument. All analyses were performed in the Microanalytical Laboratory of the Department of Analytical Chemistry at the Ruhr-University Bochum. Nitrogen sorption experiments were carried out with a Quantachrome Autosorp-1 MP, optimised protocols and gases of 99.9995% purity at 77 K. The specific surface areas were calculated by fitting the measured type I isotherms to the Langmuir and BET surface models. PXRD measurements of the samples were recorded with a D8-Advance Bruker AXS diffractometer with Cu-K_α radiation (λ = 1.54178 Å) in θ–2θ geometry, Göbel mirror; θ–2θ scan; operating at 25 °C. The instrument was equipped with a position-sensitive detector. The experimental set-up was in the capillary mode measured in Debye–Scherrer geometry. In a glove box, the samples were introduced into capillaries (0.7 mm diameter), which were then sealed prior to measurement. α-Al_2O_3 was employed as an external standard. TEM, ED, HRTEM and HAADF-STEM were carried out with a FEI Tecnai G2 microscope operated at 200 kV with an inner collection semi-angle of 90 mrad in HAADF-STEM mode. EFTEM was carried out on a JEOL 3000F microscope operated at 300 kV, equipped with a GIF 2000 postcolumn energy filter, using the standard three-window method.[32] For all techniques low intensity beam conditions (lowest possible magnification, low beam intensity and shortest possible exposure times) were used to minimise the electron dose and possible beam damage of the nanoparticle supported framework.[22] The samples were prepared in a glove box (holey carbon Cu grid, Plano, 300 mesh) and transferred to the instrument under inert conditions. XPS measurements were carried out in an ultra-high vacuum set-up equipped with a high resolution Gammadata-Scienta SES 2002 analyzer. A monochromatic Al-K_α X-ray source (1486.6 eV; anode operating at 14 kV and 45 mA) was used as incident radiation. The base pressure in the measurement chamber was around 2×10^{-10} mbar. XP spectra were recorded in the fixed transmission mode. The analyzer slit width was set to 0.3 mm and pass energy of 200 eV was chosen, resulting in an overall energy resolution better than 0.5 eV. Charging effects were compensated by applying a flood gun. The binding energies were calibrated based on the hydrocarbon C1s peak at 285 eV. Prior to individual elemental scans a survey scan was taken for all the samples in order to detect all the elements present.

Catalytic Testing

Benzyl Alcohol Oxidation: In a typical experiment, the catalytic sample (25 mg) was suspended in ultra-pure methanol (3 mL) and placed together with benzyl alcohol (1 mmol, p.a.) and K_2CO_3 (0.5 mmol) in a pressure jar. The vessel was evacuated to remove the atmosphere, filled with pure oxygen (5 bar) and heated up to 80 °C. The suspension was stirred under these conditions for 30 min. After cooling, the solution was filtered and analyzed with GC–MS. The remaining powder samples were dried in vacuo and analyzed with PXRD.

ZnO@MOF-5:[15b] The activated, guest-free MOF-5 (100 mg) and a vial containing pure liquid [(C_2H_5)$_2$Zn] (1 mL) were placed in a Schlenk tube. The Schlenk tube was evacuated to 10^{-3} mbar, sealed and kept at room temperature for about 24 h to allow adsorption. No colour change was observed. The Schlenk tube was transferred to a dry box (Ar; O_2 and H_2O below 1 ppm) for further manipulation. Because of the facile desorption of the weakly adsorbed [(C_2H_5)$_2$Zn], the vials containing the inclusion compounds [(C_2H_5)$_2$Zn]$_n$@MOF-5 were sealed and stored in a refrigerator directly attached to the glove box at –30 °C prior to further manipulation. The vials containing [(C_2H_5)$_2$Zn]$_n$@MOF-5 were transferred into a glass tube and were treated with a stream of diluted O_2 (4.5 vol.-%, 1 sccm s^{-1}, ambient pressure) in Ar at 25 °C for 6 h.

Subsequently, the samples were annealed at 250 °C under dynamic vacuum (10^{-3} mbar). Samples were stored under inert atmosphere.

TiO_2@MOF-5:[16] Pure activated MOF-5 (100 mg) was exposed to [Ti(O*i*Pr)$_4$] (1 mL) at 25 °C and 10^{-3} mbar (static conditions) for several hours allowing quantitative adsorption. The [Ti(O*i*Pr)$_4$]@MOF-5 obtained was placed in a glass tube and treated with oxygen (4.5 vol.-% in Ar, 1 sccm s^{-1}) at 220 °C for 6 h. After oxidation, the samples were annealed at 250 °C under dynamic vacuum (10^{-3} mbar). The yellowish TiO_2@MOF-5 was stored under Ar.

Au@MOF-5: (Method A) Freshly synthesised and activated MOF-5 (100 mg) and [ClAuCO] (200 mg) were placed in a Schlenk tube in two different vials. The vessel was evacuated to 10^{-3} mbar (static conditions) and heated to 50 °C. After 24 h, the loading was observed by a colour change to light violet. The precursor loaded [ClAuCO]@MOF-5 was transferred to a Schlenk tube and treated with hydrogen (99.999 vol.-%, 1 sccm s^{-1}) at 150 °C for 6 h. After the hydrolysis, the volatile by-products were desorbed at 150 °C under dynamic vacuum (10^{-2} mbar). The violet/red Au@MOF-5 was stored under Ar.

Au@MOF-5: (Method B) Freshly synthesised and activated MOF-5 (100 mg) and [ClAuCO] (200 mg) were placed in a Schlenk tube in two different vials. The vessel was evacuated to 10^{-3} mbar (static conditions) and heated up to 50 °C. After 24 h, the loading was observed by a colour change of the sample. The precursor loaded [ClAuCO]@MOF-5 was transferred to a Fisher–Porter bottle and evacuated for a very short period of time. The bottle was then filled with hydrogen (99.999 vol.-%, 2 bar) at 25 °C and heated to 100 °C for 6 h. A colour change from light violet to violet/red was observed. The Au@MOF-5 was stored under Ar.

Au/ZnO@MOF-5 and Au/TiO_2@MOF-5: Samples of metal oxide loaded MOF-5 (ZnO@MOF-5 or TiO_2@MOF-5) (100 mg) were exposed to [ClAuCO] (50 mg). The composite [ClAuCO]/metal oxide@MOF-5 material was transferred to a Fisher–Porter bottle. The bottle was filled with hydrogen (99.999 vol.-%, 2 bar) at 25 °C and heated to 100 °C for 6 h. A colour change from light violet to violet/red was observed. The doubly loaded materials were transferred to a glove box and stored under argon.

Supporting Information (see footnote on the first page of this article): PXRD of MOF-5, TiO_2@MOF-5, and ZnO@MOF-5, HRTEM image of a twinned Au nanoparticle in Au/ZnO@MOF-5, particle size distributions for Au/ZnO@MOF-5 and Au/TiO_2@MOF-5, Zn $L_3M_{45}M_{45}$ Auger spectra of MOF-5, ZnO@MOF-5 and Au/ZnO@MOF-5, results of catalytic testing.

Acknowledgments

This work was supported by the Deutsche Forschungsgemeinschaft (DFG) (Research Centre "Metal Support Interaction in Heterogeneous Catalysis", SFB-558). M. M. is grateful to the Ruhr-University Research School for supporting her doctoral thesis and as well to the Evangelisches Studienwerk e. V., Villigst for a stipend. S. T. gratefully acknowledges financial support from the Fund for Scientific Research Flanders (FWO). The authors acknowledge support from the European Union (Framework 6 program under a contract from an Integrated Infrastructure Initiative, reference number 026019 ESTEEM). The authors would also like to thank M. Lieb and S. Bendix for valuable help with GC–MS analysis.

---

[1] a) N. Klein, A. Henschel, S. Kaskel, *Microporous Mesoporous Mater.* **2010**, *129*, 238–242; b) N. L. Rosi, J. Eckert, M. Eddaoudi, D. T. Vodak, J. Kim, M. O'Keeffe, O. M. Yaghi, *Science* **2003**, *300*, 1127–1130.

[2] J.-R. Li, R. J. Kuppler, H.-C. Zhou, *Chem. Soc. Rev.* **2009**, *38*, 1477–1504.

[3] N. J. Hinks, A. C. McKinlay, B. Xiao, P. S. Wheatley, R. E. Morris, *Microporous Mesoporous Mater.* **2009**, *129*, 330–334.

[4] a) D. Farrusseng, S. Aguado, C. Pinel, *Angew. Chem. Int. Ed.* **2009**, *48*, 7502–7513; b) J. Y. Lee, O. K. Farha, J. Roberts, K. A. Scheidt, S. B. T. Nguyen, J. T. Hupp, *Chem. Soc. Rev.* **2009**, *38*, 1450–1459; c) A. Corma, H. Garcia, F. X. Llabrés i Xamena, *Chem. Rev.* **2010**, *110*, 4606–4655.

[5] a) D. Jiang, T. Mallat, F. Krumeich, A. Baiker, *J. Catal.* **2008**, *257*, 390–395; b) F. X. Llabrés i Xamena, O. Casanova, R. Galiasso Tailleur, H. Garcia, A. Corma, *J. Catal.* **2008**, *255*, 220–227; c) S. Neogi, M. K. Sharma, P. K. Bharadwaj, *J. Mol. Catal. A* **2009**, *299*, 1–4.

[6] S. Hasegawa, S. Horike, R. Matsuda, S. Furukawa, K. Mochizuki, Y. Kinoshita, S. Kitagawa, *J. Am. Chem. Soc.* **2007**, *129*, 2607–2614.

[7] K. V. Kovtunov, V. V. Zhivonitko, A. Corma, I. V. Koptyug, *J. Phys. Chem. Lett.* **2010**, *1*, 1705–1708.

[8] M. Meilikhov, K. Yusenko, D. Esken, S. Turner, G. Van Tendeloo, R. A. Fischer, *Eur. J. Inorg. Chem.* **2010**, 3701–1714.

[9] J. Juan-Alcañiz, E. V. Ramos-Fernandez, U. Lafont, J. Gascon, F. Kapteijn, *J. Catal.* **2010**, *269*, 229–241.

[10] a) H. R. Moon, J. H. Kim, M. P. Suh, *Angew. Chem. Int. Ed.* **2005**, *44*, 1261–1265; b) S. Opelt, S. Türk, E. Dietzsch, A. Henschel, S. Kaskel, E. Klemm, *Catal. Commun.* **2008**, *9*, 1286–1290; c) M. Sabo, A. Henschel, H. Fröde, E. Klemm, S. Kaskel, *J. Mater. Chem.* **2007**, *17*, 3827–3832.

[11] H.-L. Jiang, B. Liu, T. Akita, M. Haruta, H. Sakurai, Q. Xu, *J. Am. Chem. Soc.* **2009**, *131*, 11302–11303.

[12] a) S. Hermes, F. Schröder, S. Amirjalayer, R. Schmid, R. A. Fischer, *J. Mater. Chem.* **2006**, *16*, 2464–2472; b) M. Müller, O. I. Lebedev, R. A. Fischer, *J. Mater. Chem.* **2008**, *18*, 5274–5281; c) S. Proch, J. Herrmannsdörfer, R. Kempe, C. Kern, A. Jess, L. Seyfarth, J. Senker, *Chem. Eur. J.* **2008**, *14*, 8204–8212.

[13] D. Esken, X. Zhang, O. I. Lebedev, F. Schröder, R. A. Fischer, *J. Mater. Chem.* **2009**, *19*, 1314–1319.

[14] F. Schröder, D. Esken, M. Cokoja, W. E. van den Berg Maurits, O. I. Lebedev, G. Van Tendeloo, B. Walaszek, G. Buntkowsky, H.-H. Limbach, B. Chaudret, R. A. Fischer, *J. Am. Chem. Soc.* **2008**, *130*, 6119–6130.

[15] a) S. Hermes, M.-K. Schröter, R. Schmid, L. Khodeir, M. Muhler, A. Tissler, R. W. Fischer, R. A. Fischer, *Angew. Chem. Int. Ed.* **2005**, *44*, 6237–6241; b) M. Müller, S. Hermes, K. Kähler, M. W. E. van den Berg, M. Muhler, R. A. Fischer, *Chem. Mater.* **2008**, *20*, 4576–4587.

[16] M. Müller, X. Zhang, Y. Wang, R. A. Fischer, *Chem. Commun.* **2009**, 119–121.

[17] F. Schröder, S. Henke, X. Zhang, R. A. Fischer, *Eur. J. Inorg. Chem.* **2009**, 3131–3140.

[18] T. Ishida, M. Nagaoka, T. Akita, M. Haruta, *Chem. Eur. J.* **2008**, *14*, 8456–8460.

[19] D. Esken, S. Turner, O. I. Lebedev, G. Van Tendeloo, R. A. Fischer, *Chem. Mater.* **2010**, *22*, 6393–6401.

[20] J. Hafizovic, M. Bjørgen, U. Olsbye, P. D. C. Dietzel, S. Bordiga, C. Prestipino, C. Lamberti, K. P. Lillerud, *J. Am. Chem. Soc.* **2007**, *129*, 3612–3620.

[21] F. W. H. Kampers, C. W. R. Engelen, J. H. C. Van Hooff, D. C. Koningsberger, *J. Phys. Chem.* **1990**, *94*, 8574–8578.

[22] S. Turner, O. I. Lebedev, F. Schröder, D. Esken, R. A. Fischer, G. Van Tendeloo, *Chem. Mater.* **2008**, *20*, 5622–5627.

[23] I. I. Vlasov, O. Shenderova, S. Turner, O. I. Lebedev, A. A. Basov, I. Sildos, M. Raehn, A. A. Shiryaev, G. Van Tendeloo, *Small* **2010**, *6*, 687–694.

[24] S. Eustis, M. A. El-Sayed, *Chem. Soc. Rev.* **2006**, *35*, 209–217.

[25] M.-C. Daniel, D. Astruc, *Chem. Rev.* **2004**, *104*, 293–346.

[26] X. Wang, X. Kong, Y. Yu, H. Zhang, *J. Phys. Chem. C* **2007**, *111*, 3836–3841.

[27] M. A. T. Sliem, T. Hikov, Z.-A. Li, M. Spasova, M. Farle, D. A. Schmidt, M. Havenith-Newen, R. A. Fischer, *Phys. Chem. Chem. Phys.* **2010**, *12*, 9858–9866.
[28] M. Müller, A. Devaux, C.-H. Yang, L. De Cola, R. A. Fischer, *Photochem. Photobiol. Sci.* **2010**, *9*, 846–853.
[29] N. Zheng, G. D. Stucky, *Chem. Commun.* **2007**, 3862–3864.
[30] J. Gascon, M. D. Hernandez-Alonso, A.-R. Almeida, G. P. M. van Klink, F. Kapteijn, G. Mul, *ChemSusChem* **2008**, *1*, 981–983.
[31] S. S. Kaye, A. Dailly, O. M. Yaghi, J. R. Long, *J. Am. Chem. Soc.* **2007**, *129*, 14176–14177.
[32] R. F. Egerton, *Electron energy-loss spectroscopy in the TEM*, Plenum Press, New York and London, **1996**.

Received: December 9, 2010